Monthly Notices
of the
ROYAL ASTRONOMICAL SOCIETY

MNRAS **490,** 527–539 (2019)
Advance Access publication 2019 September 19

doi:10.1093/mnras/stz2633

Investigating the complex velocity structures within dense molecular cloud cores with GBT-*Argus*

Che-Yu Chen [1]★ Shaye Storm,[2] Zhi-Yun Li,[1] Lee G. Mundy,[3] David Frayer,[4] Jialu Li,[3] Sarah Church,[5] Rachel Friesen,[6,7] Andrew I. Harris,[3] Leslie W. Looney,[8] Stella Offner,[9] Eve C. Ostriker,[10] Jaime E. Pineda [11] John Tobin[6] and Hope H.-H. Chen[9]

[1]*Department of Astronomy, University of Virginia, Charlottesville, VA 22904, USA*
[2]*Harvard-Smithsonian Center for Astrophysics, Cambridge, MA 02138, USA*
[3]*Department of Astronomy, University of Maryland, College Park, MD 20742, USA*
[4]*Green Bank Observatory, Green Bank, WV 24944, USA*
[5]*Physics Department, Stanford University, Stanford, CA 94305, USA*
[6]*National Radio Astronomy Observatory, Charlottesville, VA 22904, USA*
[7]*Department of Astronomy & Astrophysics, University of Toronto, Toronto, ON M5S 3H4, Canada*
[8]*Department of Astronomy, University of Illinois, Urbana, IL 61801, USA*
[9]*Department of Astronomy, University of Texas, Austin, TX 78712, USA*
[10]*Department of Astrophysical Sciences, Princeton University, Princeton, NJ 08544, USA*
[11]*Max Planck Institute for Extraterrestrial Physics, D-85748 Garching, Germany*

Accepted 2019 September 12. Received 2019 August 23; in original form 2019 June 4

ABSTRACT

We present the first results of high-spectral resolution (0.023 km s^{-1}) N_2H^+ observations of dense gas dynamics at core scales (∼0.01 pc) using the recently commissioned *Argus* instrument on the Green Bank Telescope (GBT). While the fitted linear velocity gradients across the cores measured in our targets nicely agree with the well-known power-law correlation between the specific angular momentum and core size, it is unclear if the observed gradients represent core-scale rotation. In addition, our *Argus* data reveal detailed and intriguing gas structures in position–velocity (PV) space for all five targets studied in this project, which could suggest that the velocity gradients previously observed in many dense cores actually originate from large-scale turbulence or convergent flow compression instead of rigid-body rotation. We also note that there are targets in this study with their star-forming discs nearly perpendicular to the local velocity gradients, which, assuming the velocity gradient represents the direction of rotation, is opposite to what is described by the classical theory of star formation. This provides important insight on the transport of angular momentum within star-forming cores, which is a critical topic on studying protostellar disc formation.

Key words: stars: formation – stars: protostars – ISM: kinematics and dynamics – ISM: molecules – radio lines: ISM.

1 INTRODUCTION

Stars form in dense cores of molecular clouds (hereafter MCs). The classical theory describes star formation as a four-stage process: (1) the formation of dense cores within MCs by losing magnetic and turbulent support, (2) the collapse of gravitationally unstable cores and the formation of protostellar discs through angular momentum conservation, (3) the onset of stellar winds and bipolar outflows, and (4) the termination of infall and the birth of young stellar objects (YSOs) with circumstellar discs (Shu, Adams & Lizano 1987). Magnetic effects, turbulence, and self-gravity are considered the three key agents affecting the dynamics of star-forming process in MCs at all physical scales and throughout different evolutionary stages (McKee & Ostriker 2007). In order to understand the properties of the stars and discs, the end product of the star formation process, one must determine the properties of the dense cores, which provide the initial conditions for star formation. Velocity information within dense cores is therefore a key property that must be thoroughly investigated.

Within dense cores, infall and rotation are both important in shaping the evolution of protostellar systems. The core's rotation rate is a critical quantity in shaping the outcome of core collapse:

★ E-mail: cheyu.c@gmail.com

whether a single star or multiple system is formed (Tohline 2002), and whether a large or small disc is produced (Li et al. 2014). The angular momentum of star-forming cores is therefore an important parameter in theoretical studies of protostellar evolution (e.g. Dib et al. 2010; Chen & Ostriker 2018; Hennebelle 2018; Kuznetsova, Hartmann & Heitsch 2019). In observational studies, linearly fitted gradient of line-of-sight velocity observed across cores is commonly used to estimate a core's angular momentum, regardless of the complex nature of the core-scale velocity field (Goodman et al. 1993). Previous observations (e.g. Goodman et al. 1993; Caselli et al. 2002; Pirogov et al. 2003; Chen, Launhardt & Henning 2007; Tobin et al. 2011) as well as fully 3D MHD simulations (Li et al. 2004; Dib et al. 2010; Chen & Ostriker 2015, 2018; hereafter CO15, CO18) have found a power-law relationship between the specific angular momentum $J \equiv L/M$ (where L is the angular momentum within the core and M is the core mass) and radius R for dense cores/clumps with radii $\sim 0.005-10$ pc, that $J \propto R^{\alpha}$ with $\alpha \approx 1.5$ (see e.g. CO18). The $J-R$ correlation over a huge range of spatial scales suggests that gas motion in cores originates at scales much larger than the core size, or the observed rotation-like features may arise from sampling of turbulence at a range of scales (Burkert & Bodenheimer 2000). In fact, Pineda et al. (2019) recently resolved the specific angular momentum profile for three young objects in Perseus, showing an internal profile $J(r) \propto r^{1.8}$, which is between the expected values for solid-body rotation and pure turbulence.

However, dense cores often only have $\sim$0.1–0.2 km s^{-1} difference in projected velocity across $\sim$0.05 pc (see e.g. CO18). High velocity and angular resolution are crucial to observationally detect a signature of rotation or infall and assess the true nature of velocity structure in prestellar cores and protostellar envelopes. Also, the spatial dynamic range needs to be wide to cover gas motion at core/envelope scale, while also be able to spatially resolve the potentially complex structure within the core/envelope. A unique combination of angular and spectral resolution and fast mapping capability with full spatial scale recovery is therefore necessary for an observational study to characterize the kinematics features within dense cores.

Here, we report high-resolution observations using the recently commissioned *Argus* focal plane array on the Green Bank Telescope (GBT), which provides an unprecedented view of core-scale velocity structures that can be directly linked to how the original core material forms and falls into the protostellar system. We observed five cores, both starless and protostellar, in the Perseus MC (averaged $d \approx 300$ pc; Ortiz-León et al. 2018; Zucker et al. 2019) with the N_2H^+ J = 1–0 line, which is a reliable tracer of cold, dense gas (Bergin & Langer 1997; Caselli et al. 2002). We also observed $H^{13}CO^+$ in one protostellar and one starless core. $H^{13}CO^+$ is another dense gas tracer for regions where CO is not frozen out (outer envelope) or is released back into gas phase by heating from the central protostar (inner envelope; Vasyunina et al. 2011). We therefore use $H^{13}CO^+$ as a consistency check and focus our analysis here on N_2H^+ observations only, unless $H^{13}CO^+$ data revealed features that are not seen in N_2H^+.

The outline of this paper is as follows. We introduce our observations in Section 2.1 and briefly describe our data reduction, imaging, and spectral line fitting routines in Section 2.2. The cleaned data is further investigated in Section 3, where we derive core-scale angular momentum from average velocity gradient and compare it with previous studies (Section 3.1). Detailed velocity structures in position–velocity (PV) space are also shown (Section 3.2). Further discussions and interpretations of the data for individual targets are presented in Section 4. We summarize our results in Section 5.

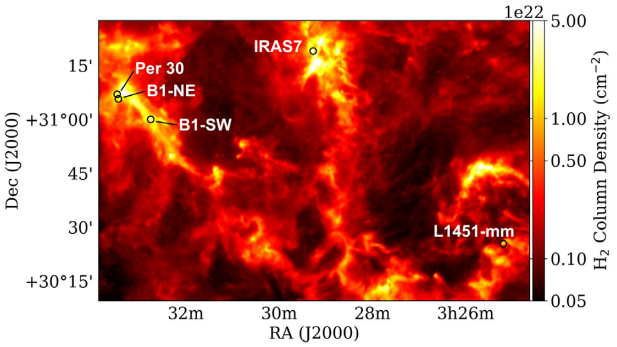

Figure 1. The Perseus molecular cloud in *Herschel* column density (André et al. 2010) with the locations of the five targets discussed in this paper.

2 DATA

Argus is a 16 pixel focal plane array operating in the 85−116 GHz range on GBT (Sieth et al. 2014), which is designed for efficient and sensitive large-area mapping. The GBT provides a beam size of $\sim$8 arcsec at 90 GHz, and *Argus* is configured in a 4 × 4 array with each pixel separated by 30.4 arcsec on the sky. Also, *Argus* has a low system temperature by using advanced monolithic millimetre-wave integrated circuit (MMIC) technology (Kangaslahti et al. 2009), which gives receiver noise temperatures of less than 53 K pixel^{-1}.

2.1 Targets and observations

Five cores in Perseus were selected for this study. Fig. 1 shows an annotated *Herschel* column density map (André et al. 2010) illustrating the locations of our targets. These cores have effective radii $\sim$20 arcsec, or about 0.03 pc at $d \approx 300$ pc, which is around the critical scale in studying the evolution of angular momentum within star-forming cores where gravitational collapse normally happens (for a review, see e.g. Li et al. 2014). The targets were chosen to cover different evolutionary stages (a mix of starless and protostellar cores) and ambient environments (cluster neighbourhood versus relatively isolated cores). Table 1 lists the basic properties of these five targets.

Observations presented here were conducted using GBT between 2017 November 18 and 2018 January 30 with the on-the-fly (OTF) method (see Mangum, Emerson & Greisen 2007, and references therein). We used the *Argus* receiver to map N_2H^+ J = 1–0 and $H^{13}CO^+$ J = 1–0 emission with the VEGAS backend. We started each session with observations of 3C 84 to adjust the telescope surface for thermal corrections, to determine pointing corrections, and to focus for the receiver. We configured the VEGAS backend to a rest frequency of 93173.704 or 86754.28840 MHz for N_2H^+ or $H^{13}CO^+$ observations, respectively, using mode 6 with 187.5 MHz of bandwidth and 1.43 kHz spectral resolution. System temperature calibration for all 16 receiver pixels was done before observing the science targets, and we performed calibration, pointing, and focus scans every 30–50 min depending on the weather. We mapped the science targets in RA and Dec. scan directions. The data were taken every 2 s with map scan rates of about 0.92 arcsec s^{-1}; this led to angular sampling of about 1.8 arcsec per sample, which was about four to five times less than the expected angular size of the beam. Frequency switching was used with offsets of −12.5 and +12.5 MHz. The beam sizes in the calibrated images are 9.4 and 9.9 arcsec for N_2H^+ and $H^{13}CO^+$, respectively.

Table 1. Summary of targets.

Target name	Region	RA (J2000)	Dec. (J2000)	1.1 mm source ID[a]	System velocity (km s^{-1})	Type
L1451-mm	L1451	03:25:10.247	+30:23:49.25	Bolo 2	4.0	Class 0
Per 30	Barnard 1	03:33:26.948	+31:06:54.89	Bolo 84	7.0	Class 0/I
B1-NE	Barnard 1	03:33:24.918	+31:05:45.92	Bolo 82	6.8	Starless
B1-SW	Barnard 1	03:32:44.367	+31:00:03.08	Bolo 70	6.8	Starless
IRAS7	NGC 1333	03:29:11.949	+31:18:30.21	Bolo 49	8.5	Triple system[b]

[a]As defined in Enoch et al. (2006).
[b]IRAS7 contains two Class 0 sources (Per 18 and Per 21) and a Class I source (Per 49).

2.2 Data reduction and spectral fitting

Argus uses the chopper wheel method for calibration, which is the standard procedure in mm and sub-mm spectral line observation (Kutner & Ulich 1981). The data is thus calibrated in $T_a{}^*$ scale, which corrects for atmospheric attenuation, resistive losses and rearward spillover and scattering. The GBT weather data base returns the atmospheric temperature and opacity information. The efficiency of *Argus* is adopted to be $\eta = 50.5$ per cent and 50 per cent for N_2H^+ (93.17 GHz) and $H^{13}CO^+$ (86.75 GHz), respectively. Note that this is the telescope efficiency associated with spatial scale of Jupiter, which is slightly larger than the primary main-beam efficiency of small, point-like sources (see the GBT Memo #302: Frayer et al. 2019). The overall uncertainty on the flux is ∼15 per cent. Nevertheless, we caution the readers that full characterization is still ongoing, and the absolute amplitude uncertainty is not used for any of the discussion below, only statistical uncertainties.

We performed standard calibration using GBTIDL including baseline subtraction, and GBTGRIDDER was used to make data cubes with pixel size 2 arcsec × 2 arcsec from maps per frequency using a Gaussian kernel. When re-gridding the data, we chose to combine 5 and 10 channels for N_2H^+ and $H^{13}CO^+$ to reach velocity resolution ≈0.023 and 0.05 km s^{-1}, respectively. The sensitivity of our final N_2H^+ maps is ∼0.15−0.25 K, and ∼0.14 K for the $H^{13}CO^+$ observation (see Table 2). We used the PYTHON package PYSPECKIT (Ginsburg & Mirocha 2011) for spectral fitting, which simultaneously fits the 15 hyperfine lines of N_2H^+ J = 1–0 and returns the fitted centroid velocity, linewidth, excitation temperature, and optical depth. We adopted a signal-to-noise cut to peak line intensity of S/N > 5 for the N_2H^+ data (S/N > 3 for $H^{13}CO^+$) when performing the fitting.

3 RESULTS

Fig. 2 summarizes our observations by showing the N_2H^+ integrated intensity maps of the observed cores. For each core, we estimate the background integrated brightness I_{bg} by sampling several intensity profiles (either along RA or Dec.) near the peak intensity I_{peak} and fitting each of them to a Gaussian function $G(x) = A\exp[-(x - x_0)^2/(2\sigma^2)]$ using the `modeling` function in ASTROPY. The background integrated brightness for the ith profile is therefore defined as $I_{bg}(i) = G_i(x \pm 2\sigma)$, and we use the median value over all $I_{bg}(i)$ as the background integrated brightness for the core. A similar procedure was applied on the *Herschel* column density data as well. These measured peak and background values are then used to draw contours in moment 0 and moment 1 maps like Figs 2–4 (and to define core boundaries; see Sections 3.1 and 3.2 below).

Table 2 lists the peak and background integrated brightness of N_2H^+ for each target. As a sanity check, we compared the measured peak intensity and system velocity with previous studies (e.g. Pineda et al. 2011; Storm et al. 2014, 2016) when possible, and found that our results are consistent with those data (after correcting for the different distances that may have been assumed). Also, one of our target, B1-SW, has also been identified as a dense core by Kirk, Johnstone & Tafalla (2007) using N_2H^+ (their core number 79), and the measured system velocity (6.8 km s^{-1}) and peak integrated intensity (∼4 K km s^{-1}) in our observation agree very well with their result.

3.1 Linear velocity gradient

Figs 3 and 4 summarize the kinematic features observed in our targets by showing maps of the line-of-sight velocity (left-hand panels), linewidth (middle panels), and PV diagrams (right-hand panels; will be discussed in Section 3.2) of these targets. Generally speaking and considering the typical gas temperature ∼10 K (c_s ≈ 0.2 km s^{-1}), almost all cores show smooth velocity structures with sub- to trans-sonic linewidths inside the cores. These zones of subsonic turbulence are usually labelled coherent cores (see e.g. Goodman et al. 1998; Pineda et al. 2010, 2015). The only exception is the triple system IRAS7 (see Fig. 4), which has a more complex velocity field at the core scale and a larger linewidth (trans- to supersonic). This implies that the IRAS7 core is more turbulent and could be a hint of turbulence-induced fragmentation within

Table 2. Summary of observations.

Target name	On-source time (h)[a]	N_2H^+ I_{peak} (K km s^{-1})	N_2H^+ I_{bg} (K km s^{-1})	N_2H^+ sensitivity (K)	$H^{13}CO^+$ I_{peak} (K km s^{-1})	$H^{13}CO^+$ sensitivity (K)
L1451-mm	1.64	4.05	0.43	0.26	–	–
Per 30	3.54/3.96[b]	5.33	0.64	0.18	0.75	0.14
B1-NE		3.45	0.45		0.24	
B1-SW	2.25	4.36	0.49	0.25	–	–
IRAS7	1.64	17.35	1.63	0.26	–	–

[a]Note that this is the integration time per *Argus* beam, and the 16 beams of *Argus* overlapped during the mapping. As a result, the centre part of the map was observed with longer total integration time than the edge of the map.
[b]Per 30 and B1-NE were observed together in both N_2H^+ (3.54 h) and $H^{13}CO^+$ (3.96 h).

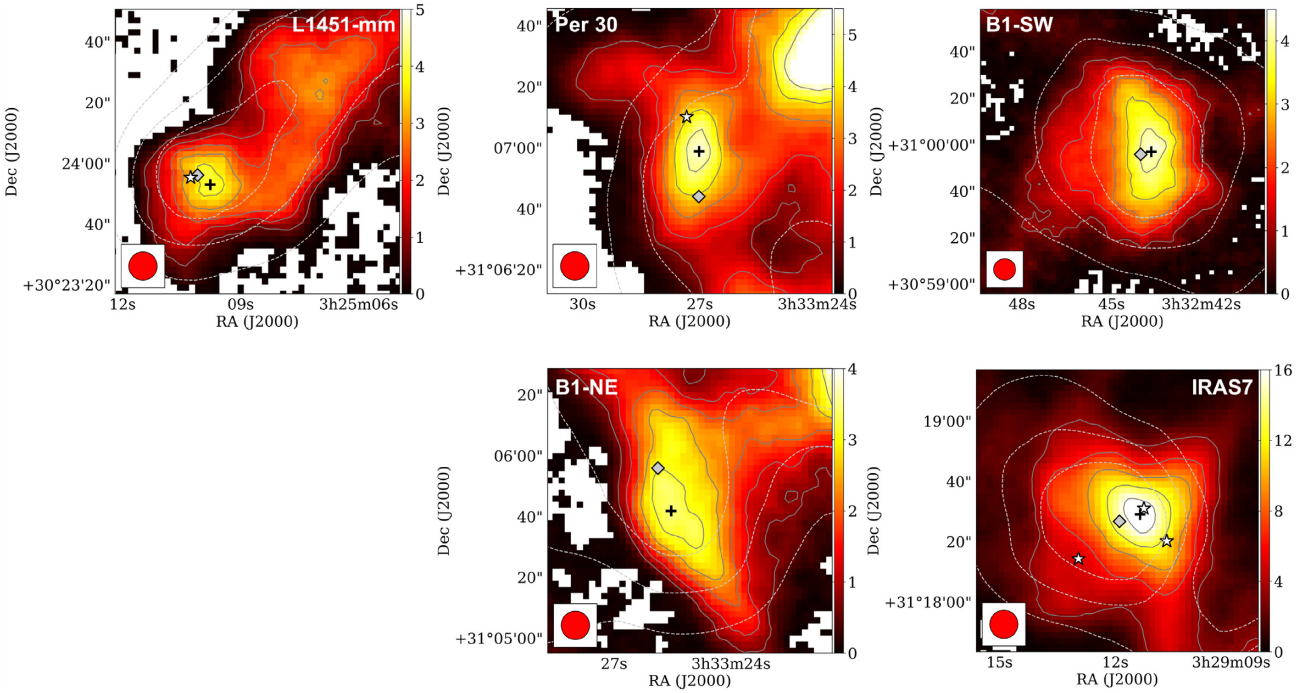

Figure 2. *Argus* N_2H^+ integrated intensity maps in K km s^{-1} (with S/N > 2 masks on PPV data cubes) of FHSC candidate L1451-mm (*top left*), protostellar core Per 30 (*top middle*), prestellar cores B1-SW (*top right*), B1-NE (*bottom middle*), and triple system IRAS7 (*bottom right*). Note that the colourscale of IRAS7 differs significantly from other panels. Known protostars (*white stars*; Enoch et al. 2009; Tobin et al. 2016) and peak locations of *Herschel* column density (*grey diamonds*) and N_2H^+ emission (*black cross*) are also marked. The contour levels are 10 per cent, 30 per cent, 50 per cent, 70 per cent, 90 per cent of ($I_{peak} - I_{bg}$) above I_{bg} for N_2H^+ integrated intensity (*grey contours*), and 25 per cent, 50 per cent, 75 per cent of ($I_{peak} - I_{bg}$) above I_{bg} for *Herschel* column density (*dashed contours*).

star-forming cores (see e.g. Offner et al. 2010, 2016; Pineda et al. 2015). Further discussions on IRAS7 are included in Section 4.4.

As a first approach of analysing the observed kinematic features, we consider the averaged linear velocity gradient at the core scale, ∇v_{lsr}. Note that we calculated the gradient of v_{lsr} at each map pixel first and averaged over the defined core region to derive ∇v_{lsr}, which is slightly different from the 2D linear fitting procedure adopted in previous studies (e.g. Goodman et al. 1993; Caselli et al. 2002; Tobin et al. 2011). When possible, we define core boundaries based on *Herschel* column density contours, since dust column density can in principle better represent the distribution of core material, not just the dense gas traced by N_2H^+. However, in cases that *Herschel* data failed to return a meaningful closed contour around the core area,[1] we adopt N_2H^+ contour levels to define cores. We would like to point out that these are indeed very rough estimates of the core boundaries, and thus are adopted for deriving the $J-R$ correlation only (see Fig. 5 and related discussions below).

Table 3 lists the velocity gradient measured from our targets, as well as the contour levels adopted as core boundaries. Each core is fitted by an ellipse to determine the effective radius of the core, $r_{core} \equiv \sqrt{a_{core} b_{core}}$, where a_{core} and b_{core} are the semilengths of the major and minor axes of the fitted ellipse, respectively. We note that, though the core boundaries and thus radii are only roughly defined, there are noticeable dependences of core shape and size on the environment: cores formed within filamentary structures (e.g. L1451-mm) tend to be more elongated (see the minor/major axes ratio b/a in Table 3), while relatively isolated cores (e.g. B1-SW and IRAS7) are more rounded and slightly bigger in size (see e.g. the moment 0 maps in Fig. 2).

The position angle of the core is also listed in Table 3 as the position angle of the major axis θ_a counterclockwise from north. The only exception is IRAS7, which is a known triple system consisting three protostars Per 18, Per 21, and Per 49. We therefore measure the velocity gradients of these three sources separately by considering circles with radius 10 arcsec (a size ∼2 × of the beam) centred at these protostars as their core boundaries. Also, for L1451-mm we adopted two different definitions of the core, which we will discuss further in Section 4.1. Nevertheless, we would like to caution the readers that though our regridded data has pixel size of 2 arcsec × 2 arcsec, our beam size is indeed 9 arcsec. This means we might only have two independent pointings across the narrowest regions of the cores, which could impact our measurements of velocity gradient. This is a common limitation of single-dish telescopes that can be alleviated with interferometers.

The linear velocity gradient at the core scale is defined as the average value of the gradient of v_{lsr} within the core. Since the fitted centroid velocity could be less accurate if the linewidth is broad,[2] we adopted a mask to only include pixels with velocity dispersion smaller than the median value within the core, $\sigma_v < \langle\sigma_v\rangle_{core}$, in determining the average linear velocity gradient for such a core. The median value is adopted as the selection criterion because it guarantees exactly half of the pixels within the core boundary

[1]Targets Per 30 and B1-NE are too close to each other and thus the resolution of *Herschel* is not good enough to well-separate them. Similarly, the triple system IRAS7 is not resolved in the *Herschel* column density map.

[2]A broad linewidth could indicate the existence of unresolved multiple velocity components along the line of sight, or potential opacity broadening if the line is optically thick.

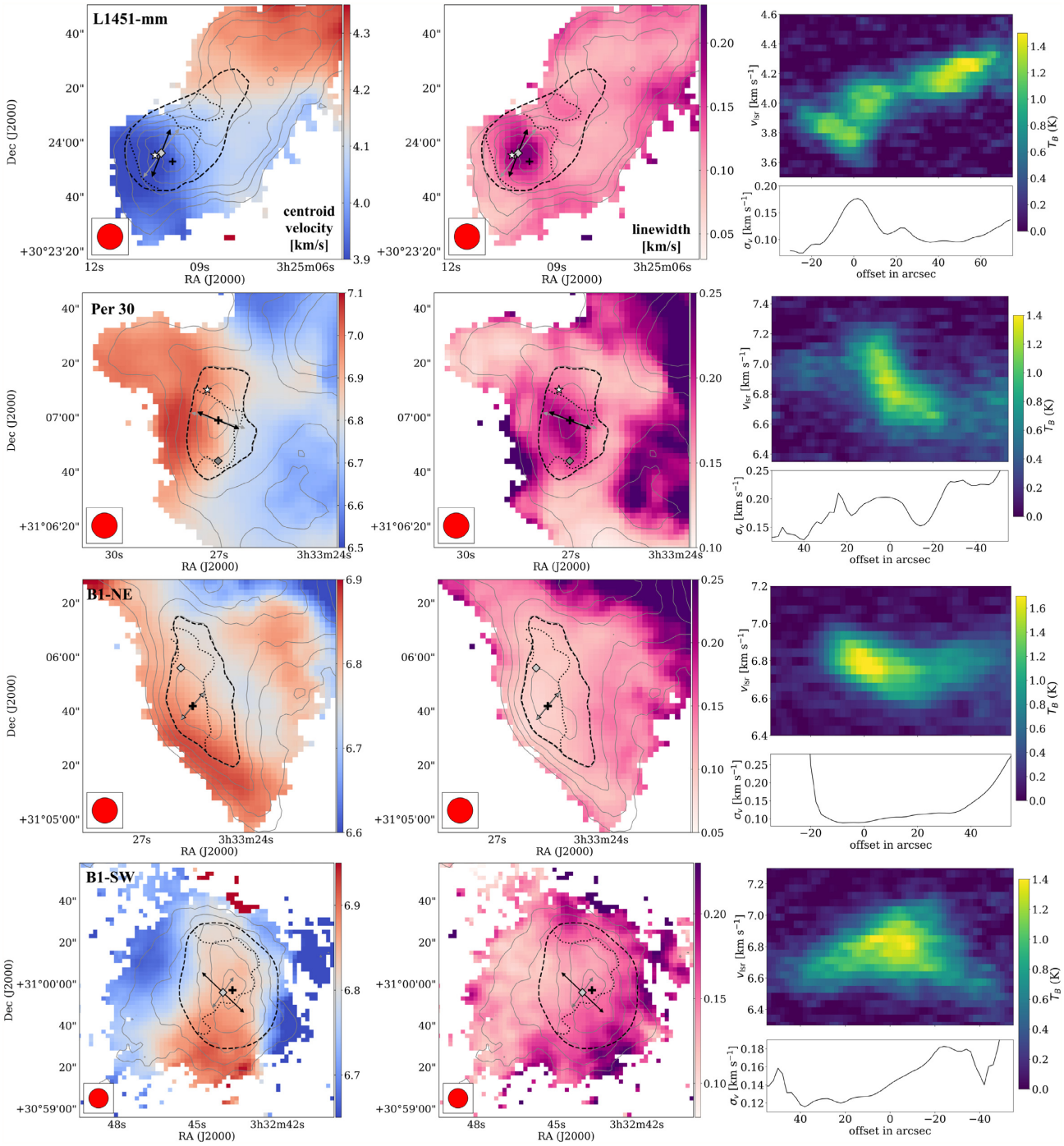

Figure 3. Maps of N_2H^+ centroid velocity (*left column*) and linewidth (σ_v; *middle column*) with N_2H^+ integrated intensity contours at the same levels as in Fig. 2, as well as the position–velocity (PV) diagrams (from the isolated N_2H^+ hyperfine line only) and position-linewidth (P–σ_v) plots (*right column*), for our targets L1451-mm (*top row*), Per 30 (*second row*), B1-NE (*third row*), and B1-SW (*bottom row*). Arrows represent the local velocity gradients averaged over the defined core area (*thick black dashed contours*; see Table 3 for definition), both with (*black*) or without (*grey*) the $\sigma_v < \langle\sigma_v\rangle$ mask (*dotted contours*). The PV diagrams and P–σ_v plots are drawn within a 20 arcsec wide zone along the black arrows, with offsets measured from the peak locations of either the *Herschel* column density (*grey diamonds*) or the N_2H^+ emission (*black cross*), depending on which one was used to define core boundaries. Known protostars are also marked as white stars.

are used, and the statistics remains relatively unaffected among cores with or without the mask. Though this selection criterion might remove the central part of the core from calculating ∇v_{lsr} as in the cases of L1451-mm, Per 30, and Per 18, we note that the purpose of finding the linear velocity gradient is to derive the angular momentum of the core, while the central part of the core usually contains more infall motions (see e.g. Section 4.1) that could potentially contaminate the measurement of core rotation.

Both values of velocity gradient with and without such masks are listed in Table 3, and their directions are illustrated in Figs 3

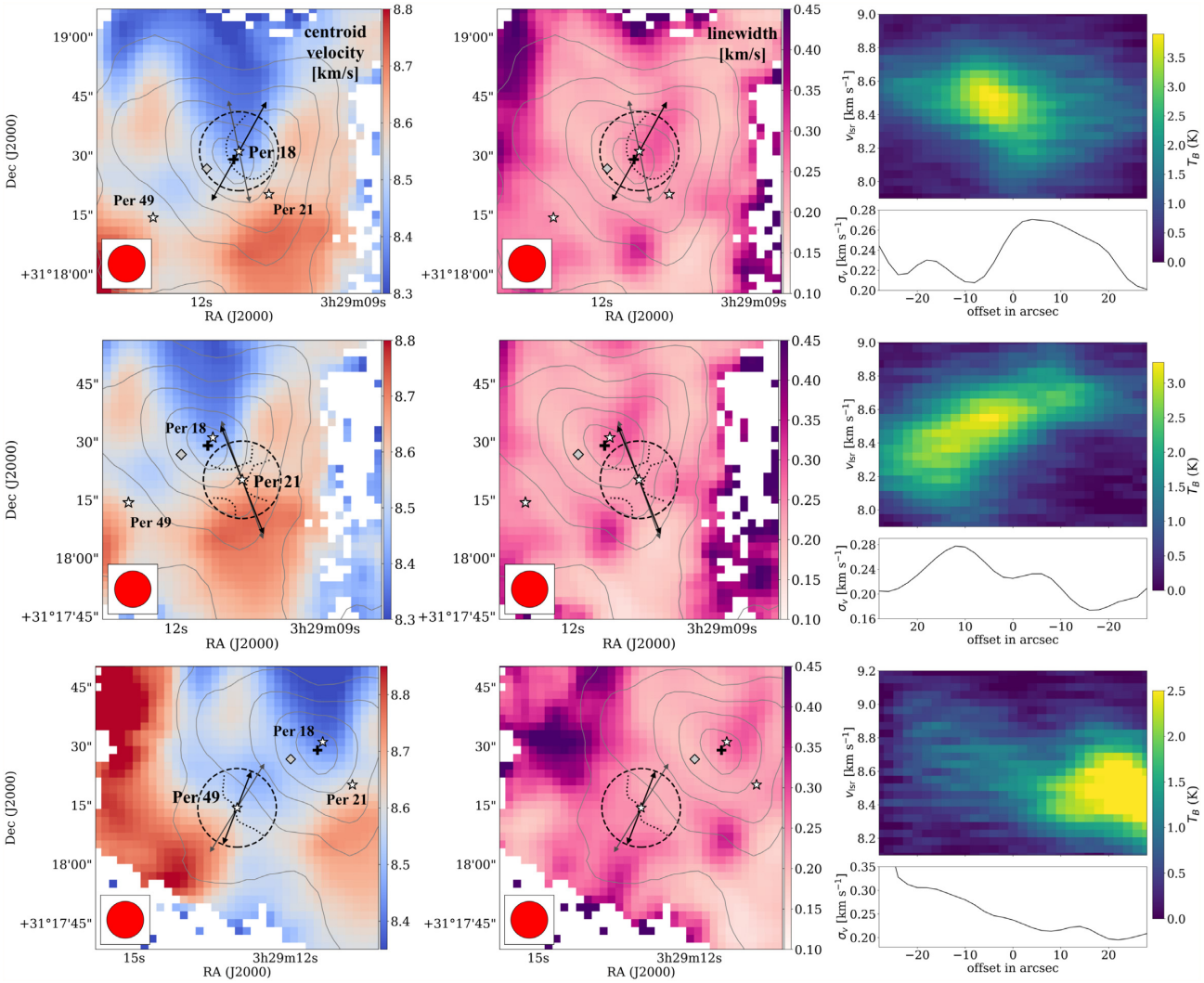

Figure 4. Same as Fig. 3 but with 10 arcsec radius circles as the core boundaries (*dashed circles*; see the text), for individual protostellar systems in IRAS7: Per 18 (*top row*), Per 21 (*central row*), and Per 49 (*bottom row*). The PV diagrams and P–σ_v plots are drawn within a 10 arcsec wide zone along the black arrows.

and 4 (black and grey arrows, respectively). One can easily see that in some cores, these linear velocity gradients are not good representatives of the overall velocity structure. The most obvious example is B1-SW, in which the derivation of linear velocity gradient with or without the $\sigma_v < \langle\sigma_v\rangle$ mask returns two directions that are almost perpendicular to each other (see the bottom row of Fig. 3). Note that the masking could also be considered a sanity check of how well the linear velocity gradient can be defined. If the masking introduces significant differences in the derived amplitude and direction of the velocity gradient (e.g. the case of B1-SW), it means the core-scale velocity structure is not best described by a linear, monotonic velocity field.

Under the usual assumption that the velocity gradient traces rotation, we can use it and the fitted core size to calculate the specific angular momentum, $J_{\rm core} \equiv L_{\rm core}/M_{\rm core} = {r_{\rm core}}^2 \nabla v_{\rm lsr}$ (see e.g. Goodman et al. 1993),[3] and compare it with the known correlation between J and core size. The results are shown in Fig. 5, where we plot measurements from previous observations (Goodman et al. 1993; Caselli et al. 2002; Pirogov et al. 2003; Chen et al. 2007; Tobin et al. 2011) as well as numerical simulations (CO15, CO18) to compare with our data.[4] Strikingly (but not surprisingly), the specific angular momenta derived from our GBT-*Argus* data fit within the previous results and the known J–R trend ($J \propto R^{\alpha}$, $\alpha \approx 1.5$) very well. However, we would like to remind the readers that though the J–R scatter plot appears to be a nice power-law correlation, it also has large uncertainties for a given radius (a factor of ∼3–5) or a given value of J (a factor of ∼10). This also means that the uncertainties in our definition of background emission and/or core boundaries will not affect the general conclusion from our comparison.

Together with the facts that (1) rotation is not the dominant motion in the simulated cores as reported in CO18 and (2) the internal velocity fields in our observed cores could be more complicated

[3]Note that we did not consider the relative angle between the velocity gradient and core shape here, as $r_{\rm core}$ is simply the geometric mean of the lengths of the major and minor axes; $J_{\rm core}$ is therefore less accurate when the aspect ratio of the core, $(b/a)_{\rm core}$, is much smaller than 1 (see Table 3).

[4]Note that the angular momenta of simulated cores in CO18 were measured in 3D, not projected 2D values.

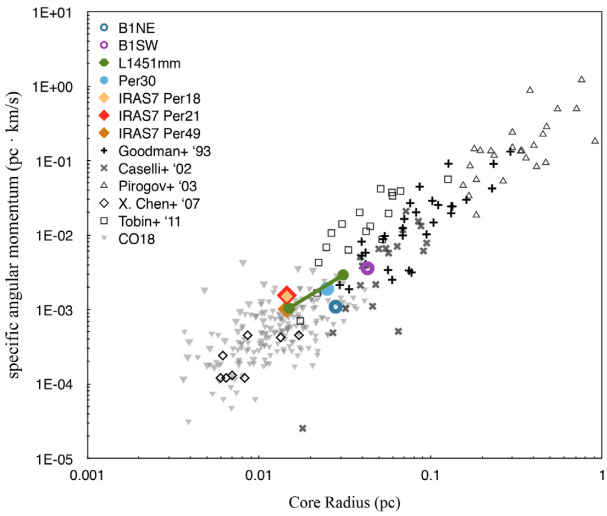

Figure 5. The specific angular momentum−radius (J−R) correlation measured in both previous observations and simulations (*black/grey symbols*), with the results of individual targets derived from this study (*coloured symbols*), adapted from CO18. Coloured open circles represent starless cores, while filled circles/diamonds represent protostellar sources. Protostars formed within the triple system IRAS7 are marked as diamonds.

than having simple, monotonic gradients (see the PV diagrams on the right-hand panels of Figs 3 and 4; also see Section 3.2 below), interpreting linear velocity gradient across the core as angular momentum from rigid-body rotation may not be appropriate. In fact, as discussed in CO18, the correlation $J \propto R^{1.5}$ can be simply treated as $\nabla v \sim \Delta v/R \propto R^{-0.5}$, or $\Delta v \propto R^{0.5}$, which agrees with the well-known property of cloud-scale turbulence in both observations and simulations (as reviewed by, e.g. McKee & Ostriker 2007). To summarize, although the so-called J−R correlation may be misleading, since J as calculated here is a proxy for angular momentum not necessarily the true angular momentum, this correlation is still real and provides a simple way to characterize a gross property of the observed velocity field. This correlation is based on directly observable quantities and should provide constraints on numerical simulations of dense cores in MCs, independent of whether or not it accurately represents the true *specific angular momentum−size* correlation.

3.2 Position–velocity diagrams

The enhanced sensitivity of GBT with *Argus* made it possible to achieve an exceptionally high-spectral resolution (0.023 km s^{-1}) in our observations, which is crucial in creating well-resolved PV diagrams. The PV diagrams of individual cores, as well as the position-averaged linewidth (P–σ_v) plots, are shown in the right-hand panels in Figs 3 and 4, which were drawn within a 20 arcsec wide zone along the direction of the averaged velocity gradient (black arrows in the $v_{\rm lsr}$ and σ_v maps in the same row), with offsets measured from either the peak values of *Herschel* column density or N_2H^+ emission (whichever was used to define the core boundary). We include the P–σ_v plots here because the linewidth contains important information on whether or not the fitted centroid velocity at each sightline is well defined. These PV diagrams and P–σ_v plots clearly show that the velocity fields within these cores are significantly more complicated than simple rigid-body rotation (see e.g. Tobin et al. 2012). In Section 4 below, we discuss in detail the observed dynamic properties of individual cores.

4 INDIVIDUAL CORES

4.1 L1451-mm

L1451-mm (also known as Per-Bolo-2; Enoch et al. 2006) is a low-mass dense core with no point-source detection in the mid-infrared (∼3−24 μm; Jørgensen et al. 2006; Rebull et al. 2007) and very low luminosity in radio wavelengths (Enoch et al. 2006). It has been classified as either a first hydrostatic core (FHSC) candidate (Pineda et al. 2011; Maureira et al. 2017), or an extremely young Class 0 protostar (Tobin et al. 2016).

Though previous observations of L1451-mm only covered the brightest core region around the N_2H^+ peak location, our GBT-*Argus* data shows that both the dense gas and velocity gradient smoothly extend to a much larger scale beyond the dense core itself (see Fig. 3). Also, the core boundary defined from *Herschel* column density contains a much larger region than the usually considered core area based on dense gas tracers only (see e.g. Pineda et al. 2011; Maureira et al. 2017), indicating that the central core is not isolated from the background gas.

To compare with previous studies that considered the N_2H^+ core only, we perform the same analysis as described in Section 3.1 on L1451-mm using the N_2H^+ 70 per cent contours (see definition in Section 3) as the core boundary. The resulting velocity gradient and PV diagram are shown in Fig. 6, and the measured core size and derived specific angular momentum are included in the J−R correlation plot, Fig. 5. Though the direction of the velocity gradient with the N_2H^+ core is 30–50° offset from that calculated within the *Herschel* core (see Table 3), the two angular momenta measured at two different scales within L1451-mm follow the power-law J−R correlation very well (see the two connected green dots in Fig. 5). This again suggests that the observed gradient in centroid velocity (which could be turbulence within the core) could be interconnected with gas motion at larger scales.

In addition, the extended emission towards the north-west part of the dense core can be clearly seen in the PV diagram in Fig. 6, which further indicates that the N_2H^+ core is dynamically associated with the surrounding gas. We note that this is similar to the observations reported by Hacar & Tafalla (2011), who found that gas velocities traced by N_2H^+ and $C^{18}O$ (which in principle traces less dense gas compared to N_2H^+) agree with each other very well. Though we do not have larger scale information and multiple density tracers as in Hacar & Tafalla (2011), the fact that gas kinematics within the central part of the core is continuous from the surrounding gas in our observation also indicates the connection between the motions within cores and at larger scales.

More importantly, from both PV diagrams (in Figs 3 and 6) we note that there clearly are two velocity components near either the protostar or the N_2H^+ peak, which could be the reason that the linewidth is significantly higher inside the N_2H^+ core than the surrounding gas (see the σ_v map and P–σ_v plot in Fig. 3). Four sample spectra (at locations marked as numbers 1–4 on Fig. 6) are shown in Fig. 7, which shows the apparent two velocity components near the N_2H^+ peak (second panel). This could be explained by radial infall broadening the line near the central region of the dense core, and the apparent two velocity components are the red- and blueshifted emission from the radial infall. Nevertheless, we note that the radial infall also could have a rotation component, or the envelope is elongated rather than spherical and thus the anisotropic infall is contributing to the velocity gradient across the source that we measured. Though the fitted centroid velocity and linewidth shown in Fig. 3 are derived assuming single velocity

Table 3. Linear velocity gradients measured in N_2H^+.

Core	Core definition	$\nabla v_{\rm lsr}$ (without $\langle\sigma_v\rangle$ mask)[a] (km s^{-1} pc^{-1})		$\theta_{\nabla v_{\rm lsr}}$ (without $\langle\sigma_v\rangle$ mask)[b] (°)		$r_{\rm core}$ (pc)	$(b/a)_{\rm core}$	θ_a[b] (°)
L1451-mm	*Herschel* 75 per cent	3.03 ± 1.77	(3.72 ± 2.17)	− 24.1	(− 40.5)	0.031	0.51	−54.9
	N_2H^+ 70 per cent	4.62 ± 1.50	(5.10 ± 1.83)	− 76.3	(− 71.7)	0.015	0.81	−76.1
Per 30	N_2H^+ 50 per cent	3.03 ± 1.05	(3.75 ± 1.52)	70.9	(76.2)	0.025	0.67	−7.3
B1-NE	N_2H^+ 70 per cent	1.39 ± 0.65	(1.36 ± 0.42)	134.6	(135.5)	0.028	0.49	18.3
B1-SW	*Herschel* 75 per cent	1.93 ± 1.59	(1.19 ± 2.41)	− 129.3	(141.2)	0.043	0.86	27.0
IRAS7 Per 18	10 arcsec circle	7.09 ± 2.68	(6.28 ± 4.25)	147.0	(− 166.3)	0.015	–	–
IRAS7 Per 21	10 arcsec circle	7.31 ± 2.29	(7.81 ± 2.70)	− 155.1	(− 157.5)	0.015	–	–
IRAS7 Per 49	10 arcsec circle	4.79 ± 2.14	(6.58 ± 3.30)	155.7	(144.3)	0.015	–	–

[a]Both $\nabla v_{\rm lsr}$ values with (*left column*) and without (*right column in parenthesis*) the $\sigma_v < \langle\sigma_v\rangle$ mask (see the text) are listed here in the format of (*mean value*) ± (*standard deviation*).
[b]Measured counterclockwise towards east from north.

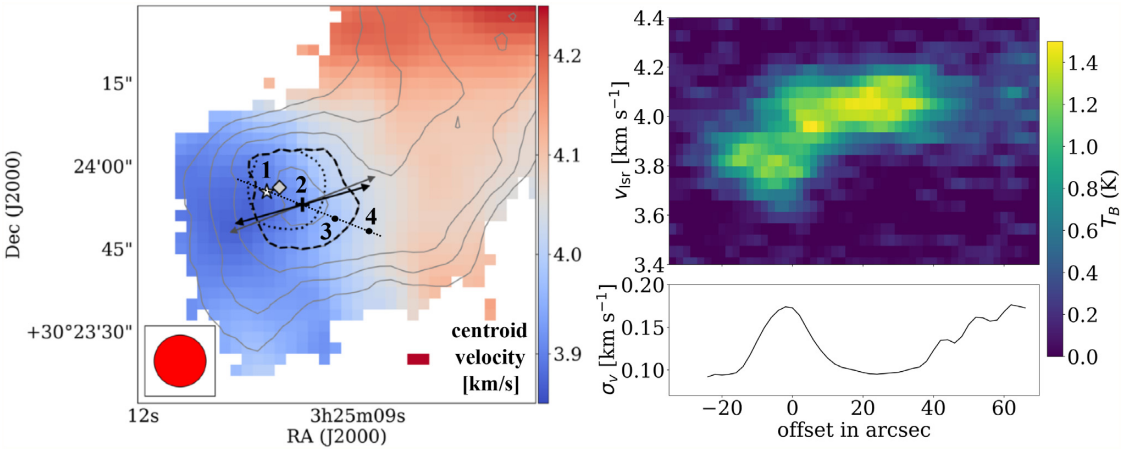

Figure 6. The centroid velocity map (*right-hand panel*) of L1451-mm, same as the top left panel of Fig. 3, but showing velocity gradients (*arrows*) derived from the N_2H^+-defined core area (*dashed contour*) and the corresponding PV diagram and P–σ_v plot (*right-hand panel*) measured along the black arrow with respect to the N_2H^+ peak (*black cross*). Numbers 1−4 marked the equally separated locations of spectra shown in Fig. 7.

components and could have errors towards the central region of the core where multiple velocity components emerge (e.g. locations 1 and 2 in Figs 6 and 7), this should not affect our measurement of the velocity gradient (and thus the J−R correlation) because we already excluded regions with broader linewidths through the σ_v mask. More discussion on spectral fitting with multiple velocity components is included in Appendix A.

Our results roughly agree with the observations reported by Maureira et al. (2017), who argued that the broad linewidth is likely caused by non-thermal motions. Together with the 'blue bulge' (blueshifted velocity in the central region of the core) seen in their velocity map, Maureira et al. (2017) suggested that these dynamic features are produced by infall motion. The 'blue bulge' is considered as a signature of infall in optically thick line emission when the redshifted emission comes only from the outer layers of the envelope and therefore has lower excitation temperature compared to the inner, blueshifted layer behind the central star (Walker, Narayanan & Boss 1994), which could result in an asymmetric velocity profile in the PV diagram with blueshifted emission being brighter (Evans 1999). Though it is not clear from our PV diagrams of L1451-mm, the spectra near the centre of the core (locations 1 and 2 in Fig. 7) do appear to have a brighter lower velocity component compared to the higher velocity one. We discuss in more detail spectral fitting with multiple velocity components and the corresponding optical depths in Appendix A.

4.2 Per 30

Per 30 (or Per-emb-30 as denoted in Enoch et al. 2009) is a Class 0/I protostar with known bipolar outflows traced by ^{12}CO (Stephens et al. 2018) and a candidate protostellar disc (Segura-Cox et al. 2018). From the velocity maps and PV diagram shown in Fig. 3, Per 30 seems to be a nice example of velocity structure produced by infall + rotation combined (see e.g. fig. 1 in Tobin et al. 2012), with linear velocity gradient at the core scale and slightly increased linewidth towards the centre of the core.

However, note that the PV diagram shown in Fig. 3 is centred at the N_2H^+ peak, not the protostar (Enoch et al. 2009; Tobin et al. 2016). The offset between the N_2H^+ peak and the protostar is $\gtrsim$10 arcsec (≈0.015 pc in Perseus), which is almost the size of typical star-forming cores, and is too large to be explained by resolution effect (considering the 7 arcsec resolution of *Spitzer* at

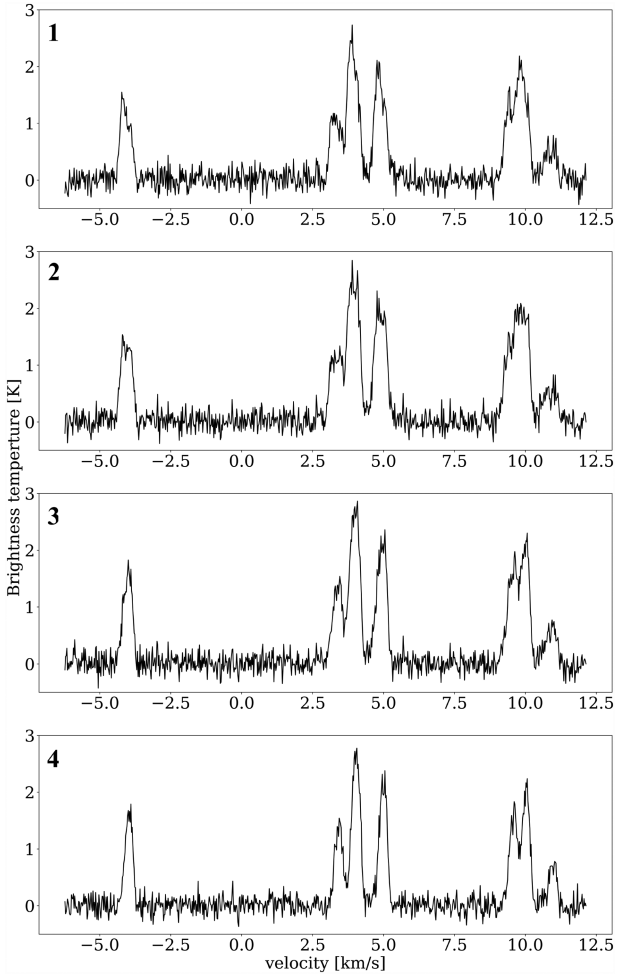

Figure 7. Spectra of L1451-mm at four equally separated locations as marked in the left-hand panel of Fig. 6, averaged over a beam. There are clearly two velocity components near the protostar (*location 1; top panel*) and the N_2H^+ peak (*location 2; second panel*) comparing to the simple, one component line profile at locations further away from the dense core (*location 4; bottom panel*).

24 μm in Enoch et al. 2009 and <1 arcsec resolution of VLA in Tobin et al. 2016), dispersal of the newly formed protostar (typically less than half of the core radius for YSOs; Jørgensen et al. 2007), or optical depth. Also, though there have been observational evidence of N_2H^+ being destroyed in warm gas surrounding the central protostar, it likely happens at smaller scales ($\lesssim$0.01 pc, or 7 arcsec at $d \approx 300$ pc; e.g. Friesen et al. 2010; Tobin et al. 2013). All of these make the 'rotation' feature doubtful.

In fact, if we re-draw the PV diagram to be centred at the peak continuum emission (determined using 1.3 mm continuum data from Stephens et al. 2018) and along the direction of local velocity gradient (calculated within the extended continuum source), we see that the N_2H^+ core could just be a clump of cold, dense gas sitting on one side of the protostar as projected on the plane of sky (see top panels of Fig. 8). Though bulk proper motion of the entire dense core is unlikely, there are observational examples showing that gas could be flowing towards the protostar along filamentary or asymmetric envelopes ('projected infall'; Tobin et al. 2011, 2012). Therefore, the N_2H^+ core could be moving towards the protostar (and thus the linear velocity gradient), or they could be totally unrelated.

The gas structure near the protostar can be more clearly seen in $H^{13}CO^+$ data, which is shown in the bottom panels of Fig. 8. We see that the $H^{13}CO^+$ data does not completely follow the N_2H^+ emission, nor is it centred around the protostar (bottom left panel in Fig. 8). However, the velocity structure is strikingly similar between these two species (see the two v_{lsr} maps in Fig. 8). We note that this is similar to the results in Punanova et al. (2018), who also found imperfect spatial correlation between N_2H^+ and $H^{13}CO^+$ within dense cores (their fig. 3), while the velocity profiles traced by these two species are highly similar (their fig. 5). Similar results were also reported in filamentary structures using N_2H^+ and $C^{18}O$ by Hacar & Tafalla (2011).

The fact that core materials with different densities have similar kinematic features could suggest that the velocity field in this region corresponds to larger scale motions and is not induced by the local rotation/infall around the protostellar system or the N_2H^+ core. In addition, from the PV diagram of $H^{13}CO^+$ centred at the protostar (bottom right panel in Fig. 8), there are clearly two spatially separated clumps of emission on the two sides of the protostar. Whether or not these $H^{13}CO^+$ clumps are real structures, and whether they contribute to the formation of the protostar, remains uncertain based on the current data.

Another feature we would like to point out is the N_2H^+ linewidth near the N_2H^+ core (see the middle and right-hand panels of the Per 30 row in Fig. 3). The P–σ_v profile shows that there are 'dips' of σ_v on the edges of the core, forming a ring-like low-σ_v region outside the N_2H^+ core, inside which the linewidth increases again towards the centre of the core. The increased linewidth near the centre of the N_2H^+ core is similar to what we observed in L1451-mm (see Section 4.1 above), which could be explained by infalling gas. However, this becomes less clear when considering that the N_2H^+ emission is far offset from the protostar, which should have the dominant gravitational field in this region.[5] At this point, it is not clear that whether the linewidth profile is providing important dynamical information or is affected by optical depth. This will be examined in our follow-up studies using detailed radiative transfer modelling to study the spectral line properties within collapsing/rotating cores.

4.3 Starless cores B1-SW and B1-NE

Two of our targets, B1-SW and B1-NE, are dense, starless cores located in the Barnard 1 region of the Perseus MC previously identified both in 1.1 mm continuum (see Table 2; Enoch et al. 2006) and N_2H^+ emission (CLASSy; Storm et al. 2014). They are classified as starless cores mainly because of the lack of point-source detection in the mid-infrared (Enoch et al. 2006, 2009).

Looking at the centroid velocity maps in Fig. 3, we clearly see that both starless cores have smooth velocity structures, with obvious velocity gradients over the observed regions. However, we first noticed that in B1-SW, the velocity gradient is not monotonic: the gas becomes more redshifted towards the bright centre of N_2H^+

[5]This would of course depend on the mass of the protostar compared to that of the N_2H^+ core. However, assuming the protostar and the core co-exist in the same local region of the MC, the fact that the protostar is at a later evolutionary stage than the core indicates that the protostar is likely more massive. In fact, a rough estimate using *Herschel* column density map gives the mass of the dense core ~0.4 $M_\odot$, while the mass of the protostellar disc around the protostar has been reported to be ~0.1−0.2 $M_\odot$ in Segura-Cox et al. (2016). Considering that a protostar is typically much more massive than its disc, this agrees with our initial guess that the gravity of the protostar dominates in this region.

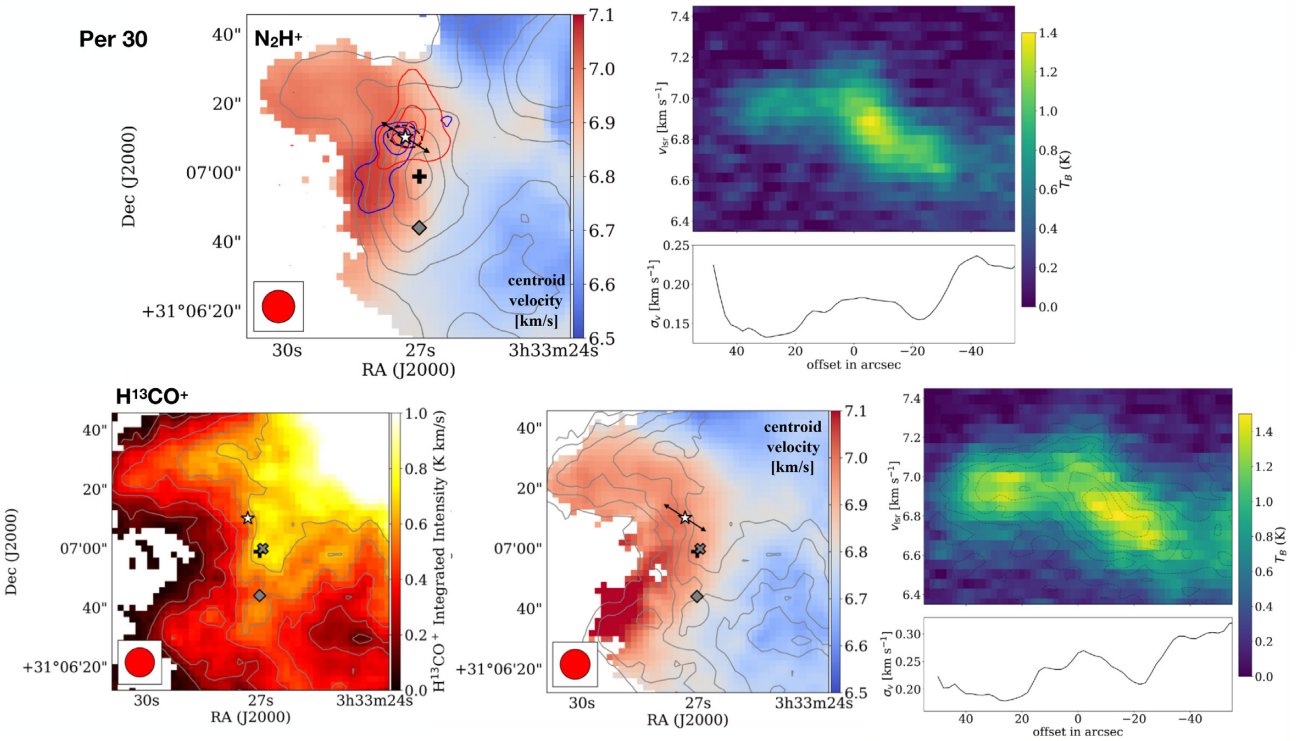

Figure 8. *Top row:* The N_2H^+ centroid velocity map of Per 30 (*left-hand panel*; same as the one in Fig. 3) with ^{12}CO outflows (*blue and red contours*; Stephens et al. 2018), and the PV diagram and P–σ_v plot (*right-hand panel*) along the velocity gradient (*black arrow*) averaged over the region with 1.3 mm emission (*dashed contour*; Stephens et al. 2018). *Bottom row:* Similar as the N_2H^+ data of Per 30 in Fig. 3, but showing $H^{13}CO^+$ data instead. The contour levels are integrated $H^{13}CO^+$ intensity at [0.16, 0.28, 0.4, 0.53, 0.65] K km s^{-1}. Grey 'x' signs mark the location of peak $H^{13}CO^+$ emission. Note that since the $H^{13}CO^+$ data is noisier than N_2H^+, we adopted the direction of velocity gradient measured in N_2H^+ around the protostar (*black arrows in the v_{lsr} maps in both rows*) to draw the PV diagram and P–σ_v plot for $H^{13}CO^+$ (*right-hand panel*), which shows two separated clumps of emission on both sides of the protostar. The distribution of N_2H^+ emission in the PV space centred at the protostar (*top right*) is overplotted as grey contours (with levels T_B = [0.2, 0.4, 0.6, 0.8, 1.0, 1.2, 1.4] K) on the PV diagram of $H^{13}CO^+$ (*bottom right*) for direct comparison.

emission from both east and west halves of the core. This is also reflected by the fact that the averaged velocity gradients with and without the narrow-line limit ($\sigma_v < \langle\sigma_v\rangle$) are almost perpendicular to each other (see the black and grey arrows in Fig. 3), because the strongest velocity gradients within the core (east to west on the east side, and west to east on the west side) are easily cancelled out and contribute little to the averaged value. This divergent gradient can be seen more clearly in the PV diagram, and B1-SW appears to have a wedge-like structure in the PV space with the brightest N_2H^+ emission located at the top (see the right-hand panel of the bottom row in Fig. 3).

Intriguingly, we found a similar feature in B1-NE. Though the velocity structure within the N_2H^+-defined core of B1-NE seems to be a smooth gradient along a single direction (north-west to south-east), towards the north-west slightly outside the core the velocity becomes redshifted, same as the south-east half of the core (see the left-hand panel in the third row of Fig. 3). This again produces a two-side velocity gradient which can be clearly seen in the PV diagram (see the right-hand panel of the third row in Fig. 3). Similar as but slightly different from the case of B1-SW, the velocity structure around the B1-NE core looks like a downward arc with an offset N_2H^+ peak on the left side of the arc.

These features suggest that both of the starless cores in our observations are located near local extremes in v_{lsr}, which is in good agreement with the results found in some of the pressure-confined cores ('droplets') using NH_3 in the L1688 region of the Ophiuchus MC (Chen et al. 2018). This could imply that starless cores form via gas flows that collide obliquely at the location where flow-compressed materials eventually become dense cores, a process seen in various numerical simulations (see e.g. Vazquez-Semadeni et al. 2000; Padoan et al. 2001; Ballesteros-Paredes et al. 2007). The origin of dense cores as a result of accretion shocks has also been discussed in Pineda et al. (2010) because of the observed sharp transition to coherence. A rough, order-of-magnitude estimate with the assumption that the momentum lost during the shock is isotropic would indicate a shock compression ratio of $\rho_{\rm post-shock}/\rho_{\rm pre-shock} \sim \mathcal{M}^2 \sim (\Delta v/c_s)^2$. Since $\Delta v_{\rm los} \approx 0.4$ km s^{-1} for both B1-NE and B1-SW (see the PV diagrams in Fig. 3), we have $\rho_{\rm post-shock}/\rho_{\rm pre-shock} \sim 4$ assuming $c_s = 0.2$ km s^{-1}. The *Herschel* column density data shows a factor of ~4–5 enhancement in $N_{\rm H}$ across the cores, which roughly agree with the shock compression ratio if we further assume the cores are formed within a locally flat region, i.e. $\Sigma_{\rm post-shock}/\Sigma_{\rm pre-shock} \sim \rho_{\rm post-shock}/\rho_{\rm pre-shock}$.

Indeed, we cannot fully rule out the possibility of gravity-induced, magnetic field-regulated (i.e. anisotropic) density enhancement within these cores. More detailed analytical analysis, numerical modelling, and synthetic observations are underway to further investigate these two scenarios and will be discussed in a follow-up paper. Future survey-style observations will also be helpful to statistically determine if the divergent velocity gradient and the arc-shape PV structure revealed in this data set are common among starless cores.

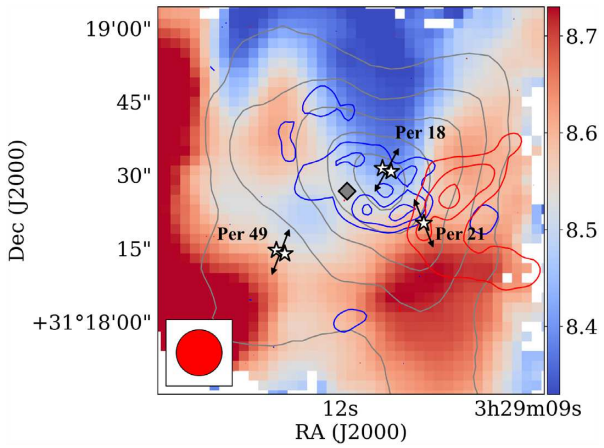

Figure 9. Illustration of the complex structure within IRAS7, showing the centroid velocity (in km s^{-1}) traced by N_2H^+ (*colourmap*) with fitted local velocity gradients (*black arrows*) same as in Fig. 4. Protostars are marked as white stars, and the outflow (mostly dominated by Per 21) traced by ^{12}CO (Stephens et al. 2018) is included (*blue and red contours*). Outflow from Per 18 has also been detected and is nearly north–south (Tobin et al. 2018). The separations of the binary systems in Per 18 and Per 49 are for demonstration only and are not drawn to scale.

4.4 IRAS7

IRAS7 is a dense core in the NGC 1333 region of Perseus (Jennings et al. 1987; Lefloch et al. 1998) which appears to be a triple system in *Spitzer* images (Enoch et al. 2009). The three protostellar components of the triple system, Per 18, Per 21, and Per 49, were later included in the VLA Nascent Disk and Multiplicity survey to study the innermost regions surrounding the protostellar sources (Tobin et al. 2016) and the Mass Assembly of Stellar Systems and their Evolution with the SMA (MASSES) survey to study gas dynamics of outflows and protostellar envelopes (Lee et al. 2016; Frimann et al. 2017; Stephens et al. 2018; Andersen et al. 2019).

A complete view of the velocity field traced by our N_2H^+ data is shown in Fig. 9, with ^{12}CO outflows (most likely from Per 21) from the MASSES survey overplotted. Note that ^{12}CO outflows from Per 18 were also detected at smaller scales ($\lesssim$3 arcsec), which is nearly north–south and edge-on (Tobin et al. 2018). Among all five targets observed in this study, IRAS7 has the most complex velocity field (see Figs 3 and 9), which can be directly linked to the clustered environment of IRAS7. Despite the disordered velocity structure at the core scale, we actually found that the three protostellar systems in IRAS7 all have simple, one-directional velocity gradients locally within the ∼20 arcsec scale (see Fig. 4) that, when interpreted as rotation, fit in the specific angular momentum−radius correlation very well (Fig. 5). In addition, the local velocity fields around the three protostellar systems seem to be interconnected spatially (Fig. 9). This is especially obvious for the pairs Per 18−Per 21 and Per 18−Per 49 by looking at the gas structures in the PV diagrams (Fig. 4), where we see the brightest N_2H^+ emission within IRAS7 (originated around Per 18) is connected to local dense gas surrounding both Per 21 and Per 49 in the PV space.

Interestingly, the two protostellar systems in IRAS7, Per 18 and Per 49, are multiple systems themselves (Tobin et al. 2016), as illustrated in Fig. 9 (not to scale). Surprisingly, these two multiple systems both have local velocity gradients perpendicular to the projected separation between the binaries. Assuming the velocity gradient is representing the rotation of local gas, this is completely opposite to what described by the classical star formation theory,[6] which envisions the flattening of dense core as the consequence of angular momentum conservation, and any sequential evolution of structures (protostellar disc, multiple system, etc.) should all take place in the plane perpendicular to the rotational axis of the core (for a review, see e.g. Tohline 2002). This could suggest that the rotation at core/envelope scales does not transfer efficiently all the way to the disc-forming scale, or the velocity gradient observed here is not generated by rotation. In fact, a recent study by Tobin et al. (2018) has shown that gas rotation in Per 18 at small scales (∼1 arcsec; see their fig. 10) is orthogonal to the local velocity gradient that we observed. However, it is worth mentioning that the binary-forming plane could also be altered by other mechanisms (e.g. turbulent accretion; interaction between forming multiple companions and local turbulence within the core) at later stages during disc formation (Pineda et al. 2015; Offner et al. 2016). Future studies on scales between 1 and 20 arcsec will help investigate the progression of gas kinematics from outer envelopes to disc-forming regions.

5 SUMMARY

Velocity information within dense cores is one of the critical properties needed to understand the star-forming process, because it provides the initial conditions for all protostellar evolution. However, there is yet not much investigation on core-scale kinematics simply because of a lack of the required combination of spatial dynamic range, spectral resolution, and sensitivity for appropriate dense core molecular line tracers. Here, we report the high-spectral resolution N_2H^+ J = 1–0 line data towards 5 dense cores (and $H^{13}CO^+$ data of Per 30) in the Perseus MC with 9 arcsec resolution and $\gtrsim$1 arcmin spatial coverage using the *Argus* focal plane array on GBT.

We summarize our main conclusions below:

(i) Spectral resolution is crucial for revealing the true dynamic features within dense cores. Though the fitted centroid velocity field may seem smooth and show a clear gradient that can be interpreted as rotation (Fig. 5), the detailed gas structure in the PV space, which is only achievable with a high-enough spectral resolution, can provide better constraints on the true nature of gas kinematics in these star progenitors (Figs 3 and 4).

(ii) Our data on L1451-mm roughly agrees with the infall scenario discussed in Maureira et al. (2017), with spectra showing multiple velocity components towards the centre of the core (Fig. 7) and the significantly larger linewidth within the dense core (top row of Fig. 3; also see Fig. 6). Moreover, the extended N_2H^+ emission on the north-west side of the core and the smooth, coherent velocity field over the $\gtrsim$1 arcmin (∼0.08 pc) gas structure suggest that the core-scale kinematics are connected to the cloud-scale gas motion.

[6]The measurable quantity here is the orientation of the line connecting the two stellar components in the sky plane. The angle between this line and the angular momentum axis of the orbit (perpendicular to the orbital plane in 3D) projected in the sky plane can have any value, depending where the secondary is in its orbit, which has the shape of an ellipse in the plane of the sky for an intrinsically circular orbit. In particular, when the companion is at a location along the minor axis of the (projected) ellipse, the orientation of the two stars in the sky plane would be the same as the orientation of the orbital angular momentum in the sky plane, which would be perpendicular to the orientation of velocity gradient. So it is plausible although unlikely that the orbital angular momentum and the velocity gradient could be consistent. The chance for one system for the secondary to locate near the minor axis of the (projected) orbit is already small. That for both to do the same is smaller.

(iii) Despite the well-ordered velocity field in the region, we found that the N_2H^+ emitting dense core near the Class 0/I protostar Per 30 (Tobin et al. 2016) may not be dynamically tied to the protostar, considering the separation between the N_2H^+ peak and the protostar is wide ($\gtrsim$ 10 arcsec) and the gas structure in the PV space seems to centre on the N_2H^+ peak instead of the protostar (Fig. 3). Additional $H^{13}CO^+$ data around Per 30 also show two separated clumps in the PV space on both sides of the protostar (Fig. 8), but whether or not this is a physical or chemical effect remains uncertain.

(iv) Both of the two starless cores observed in this study, B1-NE and B1-SW, show arc-like structures in the PV space (Fig. 3), suggesting that they may have formed near the convergent point of two oblique gas flows, a feature of the so-called turbulent model of star formation (for reviews, see Vazquez-Semadeni et al. 2000; Ballesteros-Paredes et al. 2007). This is also in good agreement with the results found in pressure-confined clumps in the L1688 region in Ophiuchus that these clumps tend to be located at local extrema of centroid velocity (Chen et al. 2018).

(v) As a triple system-forming dense core, IRAS7 shows the most complex velocity structure at the core scale (Fig. 9), though locally ($\lesssim$20 arcsec) there are simple, one-directional velocity gradients around each of the protostellar systems forming in IRAS7. Interestingly, the local velocity gradients near the two multiple systems in IRAS7, Per 18 and Per 49, are both nearly perpendicular to the projected separation between the binaries (Tobin et al. 2016). Moreover, the gas rotation in the pseudo-disc/innermost envelope of Per 18 ($\lesssim$1 arcsec) also appears to be orthogonal to the 20 arcsec scale velocity gradient (Tobin et al. 2018). This could suggest that the local velocity gradient is not induced by rotation, or that the rotation at the envelope scale is not efficiently transported to the disc-forming scale.

(vi) The kinematic features revealed in this study are intriguing, but many fundamental questions remain uncertain with only five targets observed. Future survey-style observational projects will help provide answers statistically on the origin of angular momenta within star-forming cores and the connection between core-scale and cloud-scale gas dynamics.

ACKNOWLEDGEMENTS

We thank the referee for a very helpful report. The authors would like to thank the *Argus* instrument team from the Stanford University, Caltech, JPL, University of Maryland, University of Miami, and the Green Bank Observatory for their efforts on the instrument and software that have made this work possible. The *Argus* instrument construction was funded by the National Science Foundation (NSF) ATI-1207825. Green Bank Observatory is a facility of the National Science Foundation and is operated by Associated Universities, Inc. CYC and ZYL acknowledge support from NSF AST-1815784. ZYL is supported in part by the National Aeronautics and Space Administration (NASA) 80NSSC18K1095 and NNX14AB38G and NSF AST-1716259. AIH and JL acknowledge support from NSF AST-1615647. This research made use of ASTROPY,[7] a community-developed core PYTHON package for Astronomy (Astropy Collaboration 2013, 2018).

REFERENCES

Andersen B. C. et al., 2019, ApJ, 873, 54
André P. et al., 2010, A&A, 518, L102
Astropy Collaboration, 2013, A&A, 558, A33
Astropy Collaboration, 2018, AJ, 156, 123
Ballesteros-Paredes J., Klessen R. S., Mac Low M.-M., Vazquez-Semadeni E., 2007, Protostars and Planets V. Univ. Arizona Press, Tucson, AZ, p. 63
Bergin E. A., Langer W. D., 1997, ApJ, 486, 316
Burkert A., Bodenheimer P., 2000, ApJ, 543, 822
Caselli P., Benson P. J., Myers P. C., Tafalla M., 2002, ApJ, 572, 238
Chen C.-Y., Ostriker E. C., 2015, ApJ, 810, 126
Chen C.-Y., Ostriker E. C., 2018, ApJ, 865, 34
Chen X., Launhardt R., Henning T., 2007, ApJ, 669, 1058
Chen H. H.-H. et al., 2018, ApJ, 877, 93
Dib S., Hennebelle P., Pineda J. E., Csengeri T., Bontemps S., Audit E., Goodman A. A., 2010, ApJ, 723, 425
Enoch M. L. et al., 2006, ApJ, 638, 293
Enoch M. L., Evans N. J., II, Sargent A. I., Glenn J., 2009, ApJ, 692, 973
Evans N. J., II, 1999, ARA&A, 37, 311
Frayer D. T. et al., 2019, preprint (arXiv:1906.02307)
Friesen R. K., Di Francesco J., Shimajiri Y., Takakuwa S., 2010, ApJ, 708, 1002
Frimann S. et al., 2017, A&A, 602, A120
Ginsburg A., Mirocha J., 2011, Astrophysics Source Code Library, record ascl: 1109.001
Goodman A. A., Benson P. J., Fuller G. A., Myers P. C., 1993, ApJ, 406, 528
Goodman A. A., Barranco J. A., Wilner D. J., Heyer M. H., 1998, ApJ, 504, 223
Hacar A., Tafalla M., 2011, A&A, 533, A34
Hennebelle P., 2018, A&A, 611, A24
Jennings R. E., Cameron D. H. M., Cudlip W., Hirst C. J., 1987, MNRAS, 226, 461
Jørgensen J. K. et al., 2006, ApJ, 645, 1246
Jørgensen J. K., Johnstone D., Kirk H., Myers P. C., 2007, ApJ, 656, 293
Kangaslahti P. et al., 2009, NASA Tech. Briefs, no. NPO46522. NASA, Washington D.C., USA. p. 14
Kirk H., Johnstone D., Tafalla M., 2007, ApJ, 668, 1042
Kutner M. L., Ulich B. L., 1981, ApJ, 250, 341
Kuznetsova A., Hartmann L., Heitsch F., 2019, ApJ, 876, 33
Lee K. I. et al., 2016, ApJ, 820, L2
Lefloch B., Castets A., Cernicharo J., Langer W. D., Zylka R., 1998, A&A, 334, 269
Li P. S., Norman M. L., Mac Low M.-M., Heitsch F., 2004, ApJ, 605, 800
Li Z.-Y., Banerjee R., Pudritz R. E., Jørgensen J. K., Shang H., Krasnopolsky R., Maury A., 2014, Protostars and Planets VI. Univ. Arizona Press, Tucson, AZ, p. 173
McKee C. F., Ostriker E. C., 2007, ARA&A, 45, 565
Mangum J. G., Emerson D. T., Greisen E. W., 2007, A&A, 474, 679
Maureira M. J., Arce H. G., Dunham M. M., Pineda J. E., Fernández-López M., Chen X., Mardones D., 2017, ApJ, 838, 60
Offner S. S. R., Kratter K. M., Matzner C. D., Krumholz M. R., Klein R. I., 2010, ApJ, 725, 1485
Offner S. S. R., Dunham M. M., Lee K. I., Arce H. G., Fielding D. B., 2016, ApJ, 827, L11
Ortiz-León G. N. et al., 2018, ApJ, 865, 73
Padoan P., Juvela M., Goodman A. A., Nordlund Å., 2001, ApJ, 553, 227
Pineda J. E., Goodman A. A., Arce H. G., Caselli P., Foster J. B., Myers P. C., Rosolowsky E. W., 2010, ApJ, 712, L116
Pineda J. E. et al., 2011, ApJ, 743, 201
Pineda J. E. et al., 2015, Nature, 518, 213
Pineda J. E., Zhao B., Schmiedeke A., Segura-Cox D. M., Caselli P., Myers P. C., Tobin J. J., Dunham M., 2019, ApJ, 882, 103
Pirogov L., Zinchenko I., Caselli P., Johansson L. E. B., Myers P. C., 2003, A&A, 405, 639
Punanova A., Caselli P., Pineda J. E., Pon A., Tafalla M., Hacar A., Bizzocchi L., 2018, A&A, 617, A27
Rebull L. M. et al., 2007, ApJS, 171, 447
Segura-Cox D. M. et al., 2016, ApJ, 817, L14
Segura-Cox D. M. et al., 2018, ApJ, 866, 161

[7] http://www.astropy.org

Shu F. H., Adams F. C., Lizano S., 1987, ARA&A, 25, 23
Sieth M. et al., 2014, in Holland W. S., Zmuidzinas J., eds, Proc. SPIE Conf. Ser. Vol. 9153, Argus: A 16-pixel Millimeter-Wave Spectrometer for the Green Bank Telescope. SPIE, Bellingham, p. 91530P
Stephens I. W. et al., 2018, ApJS, 237, 22
Storm S. et al., 2014, ApJ, 794, 165
Storm S. et al., 2016, ApJ, 830, 127
Tobin J. J. et al., 2011, ApJ, 740, 45
Tobin J. J., Hartmann L., Bergin E., Chiang H.-F., Looney L. W., Chandler C. J., Maret S., Heitsch F., 2012, ApJ, 748, 16
Tobin J. J. et al., 2013, ApJ, 765, 18
Tobin J. J. et al., 2016, ApJ, 818, 73
Tobin J. J. et al., 2018, ApJ, 867, 43
Tohline J. E., 2002, ARA&A, 40, 349
Vasyunina T., Linz H., Henning T., Zinchenko I., Beuther H., Voronkov M., 2011, A&A, 527, A88
Vazquez-Semadeni E., Ostriker E. C., Passot T., Gammie C. F., Stone J. M., 2000, Protostars and Planets IV. Univ. Arizona Press, Tucson, AZ, p. 3
Walker C. K., Narayanan G., Boss A. P., 1994, ApJ, 431, 767
Zucker C., Speagle J. S., Schlafly E. F., Green G. M., Finkbeiner D. P., Goodman A. A., Alves J., 2019, ApJ, 879, 125

APPENDIX A: SPECTRAL FITTING TEST WITH MULTIPLE VELOCITY COMPONENTS

To better understand the gas dynamics towards regions that potentially show features of infall motions (i.e. multiple velocity components along the line of sight), we perform spectral fitting at location 2 of L1451-mm (the peak of N_2H^+ integrated intensity; see Figs 6 and 7) with multiple (2 and 3) velocity components (an optional function of PYSPECKIT), and compare it with the original fitting result assuming a single velocity component (Fig. A1). The fitting results are summarized in Table A1. We found that though the difference is small (see the residuals in the bottom panel of Fig. A1), both of the multiple-component fits successfully return two velocity components with offset ∼0.15 km s^{-1}, consistent with what we see in the PV diagrams (see Fig. 6). The linewidths of these two velocity components are both smaller than the linewidth in the original fit, which suggests that the broader linewidths in this region when fitted with single velocity component (see Fig. 3) could be caused by overlapping multiple velocity components. We also noted that the fitted excitation temperature T_{ex} and total optical depth τ_{total} of these two velocity components are very close to the single-component fit.

More importantly, the fitting results agree with the 'blue bulge' feature suggested by Maureira et al. (2017) that the blueshifted component is brighter (higher excitation temperature). This motivated us to include the third velocity component in the fit (third panel in Fig. A1) to describe the emission from central region, which is expected to be optically thick in the 'blue bulge' picture. We found that including this optically thick, very broad emission line with centroid velocity in between the redshifted and blueshifted components does return a slightly better fit to the data by reducing the residual value down by ∼ 3 per cent of the value corresponding to the two-component fit. Though preliminary, this could provide important information when investigating the potential infall profile towards the centre of the core. More detailed spectral analysis is underway and will be discussed in a separate paper.

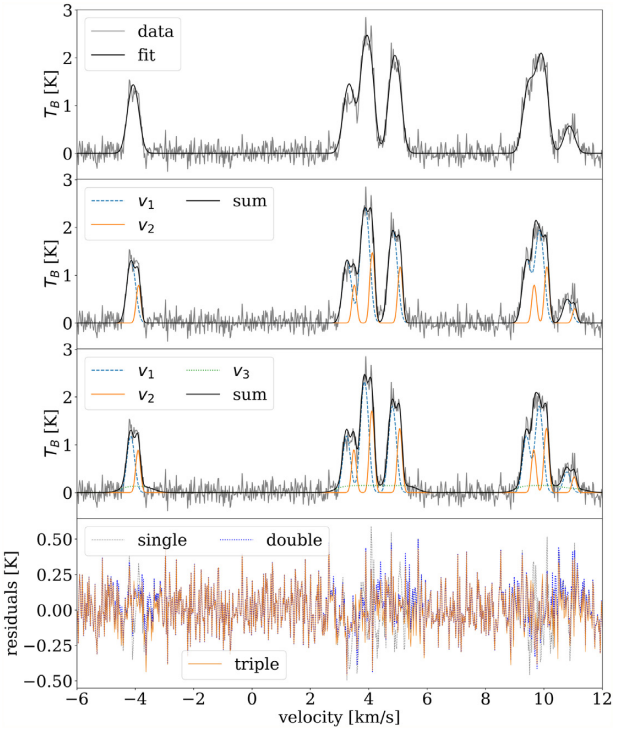

Figure A1. *Top 3 panels:* Comparison between spectral fitting results (*black*) of our GBT-*Argus* data (*grey*) at location 2 of L1451-mm (the peak of N_2H^+ integrated intensity; see Figs 6 and 7) assuming single (*top row*), double (*second row*), and triple (*third row*) velocity components. *Bottom panel:* The residual from the fits. Though the difference is small, the data is indeed better described by a multicomponent emission line.

Table A1. Spectral fitting results at location 2 of L1451-mm (the peak of N_2H^+ integrated intensity; see Fig. 6) with single, double, and triple velocity components.

Peaks	T_{ex} (K)	τ_{total}	$v_{centroid}$ (km s^{-1})	σ_v (km s^{-1})	Residual RMS
Single	5.75 ± 0.19	4.87 ± 0.51	3.967 ± 0.003	0.179 ± 0.003	0.1312
Double	6.17 ± 0.34	3.65 ± 0.53	3.898 ± 0.008	0.140 ± 0.006	0.1196
	4.98 ± 0.61	3.4 ± 1.2	4.150 ± 0.005	0.075 ± 0.005	
Triple	6.8 ± 0.7	2.57 ± 0.59	3.884 ± 0.007	0.125 ± 0.006	0.1166
	5.56 ± 0.73	2.94 ± 0.99	4.134 ± 0.006	0.077 ± 0.004	
	2.87 ± 0.03	23 ± 15	4.090 ± 0.064	0.347 ± 0.065	

This paper has been typeset from a TEX/LATEX file prepared by the author.